Tréhu, A.M., Bohrmann, G., Torres, M.E., and Colwell, F.S. (Eds.)
Proceedings of the Ocean Drilling Program, Scientific Results Volume 204

13. Geological and Geochemical Constraints on the Isotopic Composition of Interstitial Waters from the Hydrate Ridge Region, Cascadia Continental Margin[1]

H. Tomaru,[2,3] R. Matsumoto,[2] M.E. Torres,[4] and W.S. Borowski[5]

ABSTRACT

The isotopic compositions of interstitial waters collected from Hydrate Ridge during Ocean Drilling Program Leg 204 were measured to evaluate the fluid evolution of this accretionary prism. At shallow depths, the dissolved Cl^- concentrations and δD and $\delta^{18}O$ values of the interstitial water reflect changes in the salinity and the isotopic compositions of seawater from the Last Glacial Maximum to the present. The presence of disseminated gas hydrates, which is well identified by discrete low Cl^- anomalies within the gas hydrate stability zone, is accompanied by high δD and $\delta^{18}O$ values of the freshened fluids. This is consistent with incorporation of heavy isotopes into the gas hydrate lattice, which is also apparent in the signals observed at the ridge summit. Here, massive gas hydrate formation in the upper 20 meters below seafloor leads the formation of brines with dissolved Cl^- concentrations as high as 1400 mM. The interstitial waters sampled near massive gas hydrates at the ridge summit are extremely depleted in D and ^{18}O. Clay mineral dehydration within the deep prism results in a progressive decrease in Cl^- and δD with depth. Dehydration temperature estimates based on those data likely suggest a progressive increase in the temperature of isotopic fractionation between clay and water with distance from the prism toe. The oxygen isotope data probably reflect the combined effects of clay dehydration, carbonate precipitation, and alter-

[1]Tomaru, H., Matsumoto, R., Torres, M.E., and Borowski, W.S., 2006. Geological and geochemical constraints on the isotopic composition of interstitial waters from the Hydrate Ridge region, Cascadia Continental Margin. *In* Tréhu, A.M., Bohrmann, G., Torres, M.E., and Colwell, F.S. (Eds.), *Proc. ODP, Sci. Results,* 204, 1–20 [Online]. Available from World Wide Web: <http://www-odp.tamu.edu/publications/204_SR/VOLUME/CHAPTERS/109.PDF>. [Cited YYYY-MM-DD]

[2]Department of Earth and Planetary Science, University of Tokyo, 7-3-1 Hongo, Bunkyo-ku Tokyo 113-0033, Japan.
[3]Present address: Department of Earth and Environmental Sciences, University of Rochester, 227 Hutchison Hall, Rochester NY 14627, USA. **hitoshi@earth.rochester.edu**
[4]College of Oceanic and Atmospheric Sciences, Oregon State University, 104 COAS Administration Building, Covallis OR 97331-5503, USA.
[5]Department of Earth Sciences, Eastern Kentucky University, 521 Lancaster Avenue, Roark 103, Richmond KY 40475-3102, USA.

Initial receipt: 27 January 2005
Acceptance: 7 February 2006
Web publication: 6 July 2006
Ms 204SR-109

ation of oceanic basement; however, there are not enough data to constrain the relative contribution of these processes to the observed signals.

INTRODUCTION

The chemistry of interstitial water is strongly influenced by tectonic, sedimentological, mineralogical, and diagenetic processes. Dissolved chloride concentrations (Cl^-) and the stable isotope compositions (δD and $\delta^{18}O$ values) of waters are valuable in establishing the origin and evolution of fluids in marine sediments (e.g., Dählmann and de Lange, 2003; Hesse, 2003). In the absence of gas hydrates, chloride is not involved in geochemical reactions in shallow sediments. Water is the carrier of dissolved ions, and its isotopic signal reflects processes such as dehydration and gas hydrate formation involving uptake and release of water. These are the only processes that affect the hydrogen isotopic signal because water is the main hydrogen reservoir. Oxygen, however, is a major component of minerals; thus, isotopic exchange of these phases with pore water may provide valuable information on diagenetic processes.

At Hydrate Ridge, offshore Oregon (USA), the Cl^- distribution in interstitial waters within the gas hydrate stability zone (GHSZ) is clearly associated with gas hydrate dynamics, whereas at depth, the Cl^- signal reflects dehydration reactions (Torres et al., 2004a, 2004b). The migration of deep fluids to the GHSZ is a process that delivers dissolved methane for the formation of gas hydrates; thus, defining the geological and geochemical histories recorded in the interstitial waters is an essential approach for further understanding of gas hydrate systems. Here we present hydrogen and oxygen isotope data of interstitial waters from the Cascadia accretionary complex collected during Ocean Drilling Program (ODP) Leg 204 to identify key geological and geochemical processes operating within this accretionary margin.

GEOLOGICAL SETTINGS

Hydrate Ridge is a 25-km-long and 15-km-wide ridge located offshore Oregon (Fig. **F1A**) where Juan de Fuca plate obliquely subducts beneath North American plate (MacKay et al., 1992; MacKay, 1995; Goldfinger et al., 1997). Sediments in the vicinity of the ridge are composed of actively folded and faulted turbidites and hemipelagic sediments (Tréhu, Bohrmann, Rack, Torres, et al., 2003). Massive gas hydrates are observed near the seafloor and in the subsurface to a depth of ~50 meters below seafloor (mbsf) on the ridge summit, and pervasive bottom-simulating reflectors (BSRs) occur from the summit to the flanks and into the eastern slope basin of the ridge, indicating the presence of free gas underlying the subsurface gas hydrates in these sediments (Tréhu et al., 2004). Authigenic carbonates and chemosynthetic communities have also been observed at the southern peak of the ridge, where methane gas is discharged episodically into the overlying water (Torres et al., 2002; Suess et al., 1999; Heeschen et al., 2003).

F1. Leg 204 maps, p. 12.

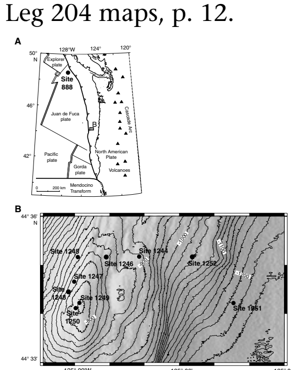

MATERIALS AND METHODS

Southern Hydrate Ridge was drilled and cored during Leg 204 in 2002 (Tréhu, Bohrmann, Rack, Torres, et al., 2003) (Fig. F1B). Three sites (Sites 1248, 1249, and 1250) were drilled at the ridge summit. Of these sites, Site 1250 has the deepest penetration and recovered ~180 m of sediments of Holocene to early Pleistocene age. The sediment is mainly composed of clay to silty clay with biogenic components, with turbidite layers intercalated as minor lithologies of the core. Three sites (Sites 1245, 1246, and 1247) were drilled at the northern and western flanks of the ridge. Site 1245 was cored deepest to a depth of ~530 mbsf. The upper sediments (~30 mbsf) at Site 1245 are mainly composed of clay with authigenic carbonate and foraminifer-rich interlayers and are devoid of gas hydrates. These sediments are underlain by diatom- or nannofossil-rich clay to silty clay with frequent sand-rich turbidites and some volcanic ash layers. At the eastern slope basin of the ridge (Sites 1244, 1251, and 1252), Site 1251 was cored deepest to a depth of ~440 mbsf in Holocene to upper Pliocene sediments. The sediment sequence is mostly composed of clay to silty clay with several turbidite and debris flow layers. The sequence between 130 and 300 mbsf at Site 1251 is enriched in siliceous and calcareous biogenic components; the deeper stratigraphic section is composed of partly lithified clay to claystone with glauconite grains and authigenic carbonate of various morphologies. Site 1252 is the only one of the nine drilled sites where no BSR is observed.

Whole-round sediment intervals (10–20 cm in length) were sampled soon after recovery according to standard ODP protocol. These were carefully skinned to remove potential seawater contamination during recovery and squeezed to extract interstitial water samples using a Manheim-type squeezing system. In addition, other water samples were collected from dissociated massive gas hydrate samples, gas hydrate–bearing sediments (sometimes identified by soupy or moussy texture), and dry-looking sediments near gas hydrate occurrences.

Dissolved chloride concentration was determined onboard by titration with silver nitrate with a precision better than 0.4% (Torres et al., 2004a). Aliquots of water samples were sealed in glass vials for postcruise stable isotope analyses at the University of Tokyo (Japan). The δD values were measured by the chromium-reduction method of Gehre et al. (1996) using the automated hydrogen preparation system, H/Device of Finnigan, equipped with MAT 252 Finnigan mass spectrometer. Results are reported in permil (‰) delta notation relative to Standard Mean Ocean Water (SMOW). Analytical precision is better than ±0.5‰. The $\delta^{18}O$ values were measured by the CO_2-equilibrium method of Epstein and Mayeda (1953) with a MAT 252 mass spectrometer. Results are reported in delta values relative to SMOW with an analytical precision better than ±0.15‰.

T1. Hydrogen and oxygen isotopic compositions, p. 18.

RESULTS AND DISCUSSION

Hydrogen and Oxygen Isotopic Compositions

Water isotopic compositions from Leg 204 are listed in Table T1 and shown in Figure F2, which includes data from Site 888 located west of the deformation front of Cascadia margin (Kastner and Elderfield, 1995). Similar to the approach used by Tréhu et al. (2004) to estimate in

F2. Dissolved Cl^-, δD, and $\delta^{18}O$, p. 13.

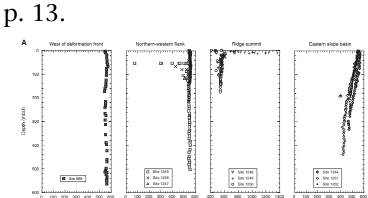

situ Cl^- values, the background levels of δD and $\delta^{18}O$ can be defined by interpolating values from the interstitial waters collected from sediments devoid of gas hydrates. (Fig. **F3**). The chemistry of such water is assumed to be free from the effects of gas hydrate formation and dissociation, and thus should reflect in situ values.

F3. Discrete Cl^- excursions, p. 16.

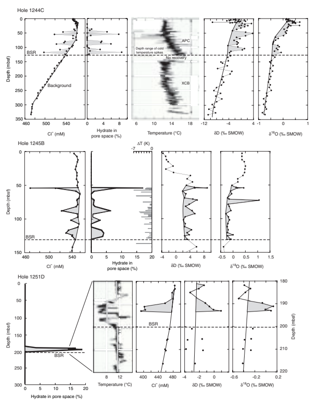

The δD values at the summit and flank sites increase from –5‰ near the seafloor to +5‰ at ~20 mbsf, show a very slight decrease downward, and then remain almost constant at values ranging from 0 to +4‰ (Fig. **F2B**). On the other hand, δD values in the slope basin decrease steeply downward, reaching values of about –10‰, and remain almost constant below 220 to 300 mbsf, with maximum values as high as +5‰ at ~20 mbsf. Positive (up to +20‰) and negative (up to –10‰) excursions in δD at all sites always accompany depletion and enrichment in Cl^- (Fig. **F2A**), respectively.

The $\delta^{18}O$ values increase from 0‰ near the seafloor to +0.5‰ at ~20 mbsf at all sites, and then decrease downward, approaching approximately –0.3‰ below 100 mbsf at the summit and flank sites, whereas they gradually decrease to values as low as –0.8‰ and become constant below 220 to 300 mbsf in the slope basin (Fig. **F2C**). Positive (up to +2.4‰) and negative (up to –0.9‰) excursions in $\delta^{18}O$ at all sites correspond with δD excursions and with anomalous depletion and enrichment in Cl^-, respectively.

Anomalies Associated with Gas Hydrate

The “spiky” decreases of dissolved Cl^- observed within the GHSZ (e.g., Holes 1244C, 1245B, and 1251D in Fig. **F3**) are accompanied by increases in δD and $\delta^{18}O$. These discrete anomalies are clearly associated with gas hydrate dissociation during core retrieval. Because the gas hydrate lattice excludes dissolved ions and preferentially incorporates D and ^{18}O during formation, the interstitial water released from gas hydrate as it dissociates shows low Cl^- concentration and high δD and $\delta^{18}O$ values in direct proportion to hydrate content (Egeberg and Dickens, 1999; Hesse et al., 2000; Matsumoto and Borowski, 2000). Conversely, strong enrichment in Cl^- in shallow depths at Site 1249 at the ridge summit may reflect rapid gas hydrate formation, which exceeds the rate at which ions can be removed by diffusion from the loci of hydrate formation (Torres et al., 2004a) or great reduction of sediment pore space due to massive gas hydrate formation, which leads to decrease of dissuasive loss of Cl^- (Milkov et al., 2004). The briny residual waters show negative excursions in δD and $\delta^{18}O$ because the water is depleted in D and ^{18}O because of isotopic fractionation during gas hydrate formation.

F4. Cl^-, δD, and $\delta^{18}O$, p. 17.

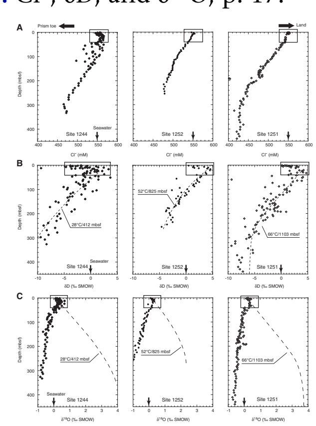

Glacial Signals in the Shallow Interstitial Waters

Sites away from the ridge crest show curvature in Cl^-, δD, and $\delta^{18}O$ in shallow sediments (e.g., Sites 1244, 1251, and 1252 as shown in the boxes in Fig. **F4**). Small positive peaks in Cl^- (Fig. **F4A**) in comparison with seawater are observed shallower than 40 mbsf in Holocene to Pleistocene sediments (Tréhu, Bohrmann, Rack, Torres, et al., 2003) and correspond with positive peaks in δD (Fig. **F4B**) and $\delta^{18}O$ (Fig. **F4C**). The methane concentration in the shallow sediments drilled away from the ridge summit is not sufficient to form gas hydrate at these depths (Milkov et al., 2003); thus, the upper ~40 mbsf of these sites are devoid of gas hydrates, as shown by analyses of multiple gas hydrate proxies (Fig. F3) (Tréhu et al., 2004). The observed synchronous changes in dissolved Cl^- and water isotopes in the upper sediments (Fig. F4) are therefore not caused by processes related to gas hydrate formation; rather, these profiles reflect the burial of seawater during glacial intervals which is enriched in dissolved ions, D, and ^{18}O because of ice sheet development (e.g., Adkins et al., 2002).

Detailed analyses of interstitial waters recovered from the Pacific, Southern, and Atlantic oceans show a Cl^- increase of ~2.6% and a $\delta^{18}O$ rise of 0.8‰ (McDuff, 1985; Schrag et al., 1996; Adkins et al., 2002), which has been used to constrain seawater temperature and salinity values from the Last Glacial Maximum (LGM) to the Holocene. In Cascadia continental margin sediments, dissolved Cl^- shows an increase of ~3.6% (Fig. F4A) and $\delta^{18}O$ increases by ~0.7‰ (Fig. F4C) relative to modern seawater. Our data set provides the first δD values associated with the postulated interstitial water records of ice volume change in glacial to interglacial timescales. We show a maximum increase in δD of ~4‰ (Fig. F4B) in the upper 40 mbsf, which is about six times greater than that observed for $\delta^{18}O$. This magnitude is consistent with the experimental results of oxygen and hydrogen isotopic fractionation for an ice-water system (O'Neil, 1968) and suggests that the observed coupled increase in δD and $\delta^{18}O$ is due to the development of ice sheet resulting in the sea level drop during the LGM. The effects of older glacial-interglacial periods in deeper interstitial waters are likely overwritten by diffusion and advection of deeper fluids.

Fluid Provenance Inferences for Interstitial Water from Cl^- and δD Profiles

The similarity in profiles of Cl^- and δD (Fig. F2) suggests that same processes control the vertical distributions of these species; both Cl^- and δD generally decrease with depth in the slope basin, whereas those remain almost constant at the other sites. Anaerobic methane oxidation (e.g., Borowski et al., 1996),

$$CH_4 + SO_4^{2-} \rightarrow HS^- + HCO_3^- + H_2O, \quad (1)$$

provides water depleted in D because the hydrogen in water can be linked to bacterially generated methane with δD values of approximately –200‰ (Coleman et al., 1981; Waseda and Uchida, 2002). Therefore, this process can decrease both Cl^- and δD. But the methane concentration is negligibly small compared with the amount of hydrogen in water (Dählmann and de Lange, 2003), and the sulfate reduction zone in Hydrate Ridge is very shallow (generally <15 mbsf) (Tréhu, Bohrmann, Rack, Torres, et al., 2003); thus, this process cannot account for the magnitude of the observed decrease in δD in deep sediments.

Membrane filtration of clay minerals causes interstitial waters to be depleted both in Cl^- and D as well as ^{18}O. Experiments have shown that Cl^- concentration can decrease by 18% and 30% in water filtered through bentonite at pressures of 14 and 28 MPa, respectively (Kharaka and Berry, 1973). In addition, Coplen and Hanshaw (1973) showed that this process results in depletion of D by 2.5‰ and depletion of ^{18}O by 0.8 ‰ when water is filtered through montmorillonite at 33 MPa. But membrane filtration, which has been shown experimentally to cause freshening and depletion in the heavy isotopes, has never been documented unambiguously in a large-scale field example (Hanor, 1987). In the slope basin at Hydrate Ridge, we observe decreases of 12%–23%, 5‰–10‰, and 0.5‰–1‰ from seawater values of Cl^-, δD, and $\delta^{18}O$, respectively (Fig. **F2**). If we assume that these values are due to membrane filtration at depth followed by fluid migration to shallower sedimentary section, the expected water isotopic fractionation observed in the above experiments are too small to cause the large depletion of D and ^{18}O in the interstitial waters.

However, water released during clay mineral diagenesis is a promising explanation for overall decreases in Cl^- and δD observed in the eastern slope basin of the ridge. Torres et al. (2004b) explain the progressive freshening of fluids landward as resulting from dehydration of smectite beneath the accreted mélange and subsequent migration of fluids from depths below 1000 mbsf where in situ temperature is >70°C. Hydrogen isotopic fractionation between smectite and water has been determined by Capuano (1992) using the relationship

$$1000 \ln \alpha^{H}_{clay\text{-}water} = \{[-45.3(10^3)]/T\} + 94.7, \qquad (2)$$

where $\alpha^{H}_{clay\text{-}water}$ is the isotopic fractionation factor of hydrogen between smectite and water and T is the fractionation temperature in degrees K. If we assume that the observed decrease in background level of Cl^- is caused by input of freshwater evolved from smectite dehydration at greater depth, we can estimate average isotopic fractionation temperature between clay and water using a mass balance calculation such that

$$X_{clay}\delta_{clay} + (1 - X_{clay})\delta_{SW} = \delta_{IW}, \qquad (3)$$

where X_{clay} is the volume fraction of water from clay mineral dehydration calculated from Cl^- change and δ_{clay}, δ_{SW}, and δ_{IW} represent the δD values of water released by dehydration, seawater, and the predicted composition of the interstitial water, respectively. Using Equations 2 and 3, we can estimate the average temperatures of hydrogen isotopic fractionation between clay and water that fit to the observed decreasing δD profiles in the slope basin. The results indicate that in situ interstitial waters were released from clay minerals isotopically exchanged at average temperatures of 28°, 52°, and 66°C at Sites 1244, 1252, and 1251, respectively, as dashed lines in Figure **F4B.** Using the regional geothermal gradient for these sites (Tréhu, Bohrmann, Rack, Torres, et al., 2003), these temperatures correspond to subbottom depths of 412, 825, and 1103 mbsf, respectively. These temperatures are too low for dehydration to occur (e.g., Perry and Hower, 1970; Pytte and Reynolds, 1989) and must reflect previous fractionation of interlayer water with the pore fluids at depth during burial, so we are not starting out with seawater values in our Equation 3. Nevertheless, the apparent temperature increases landward in the slope basin, consistent with our conceptual understanding of prism evolution based on models developed for the Barbados wedge (Bekins et al., 1994).

Causes of Depletion in ^{18}O

Decreases in Cl^- and δD values are observed only in the eastern slope basin; $\delta^{18}O$ values, however, decrease at all sites. Clay mineral dehydration in the slope basin also affects the oxygen isotopic composition of the interstitial water. The temperature dependence of isotopic fractionation of oxygen between smectite and water was determined by Savin and Lee (1988) and is given by

$$1000 \ln \alpha^{o}_{\text{clay-water}} = \{[2.60(10^6)]/T^2\} - 4.28, \quad (4)$$

where $\alpha^{o}_{\text{clay-water}}$ is the isotopic fractionation factor of oxygen between smectite and water and T is the fractionation temperature in degrees K. Such clay minerals are enriched in ^{18}O and increase $\delta^{18}O$ of interstitial water during dehydration (e.g., Dählmann and de Lange, 2003). Dashed lines in Figure **F4C** show the predicted initial background levels for $\delta^{18}O$ of the water isotopically exchanged with clay at temperatures of 28°, 52°, and 66°C at Sites 1244, 1252, and 1251, respectively, if it was derived by clay mineral dehydration. The observed decreases in $\delta^{18}O$ profiles do not follow the predicted trends; thus, the $\delta^{18}O$ values in the slope basin were generated by the combined processes of clay mineral dehydration and other geochemical reactions. The actual ^{18}O depletion in the slope basin due to reactions other than clay mineral dehydration must be greater than that at the summit and flank sites; a $\delta^{18}O$ decrease of ~5‰ in the slope basin (Fig. **F4C**) and ~0.3‰ at the other sites (Fig. **F2C**) occurs because the $\delta^{18}O$ values in the slope basin were potentially increased by the clay mineral dehydration to the values indicated as the dashed lines in Figure **F4C.**

Carbonate precipitation is an important process that can decrease $\delta^{18}O$ of interstitial water independent of δD and is described by the following general reaction:

$$M^{2+} + 2HCO_3^- \rightarrow MCO_3 + H_2O + CO_2, \quad (5)$$

where M is Ca^{2+} or Mg^{2+}, representing the formation of calcite or dolomite. The isotopic fractionation factors ($\alpha^{o}_{\text{carbonate-water}}$) of oxygen between carbonates and water are experimentally determined as calcite,

$$1000 \ln \alpha^{o}_{\text{calcite-water}} = \{[2.78(10^6)]/T^2\} - 3.39, \quad (6)$$

from O'Neil et al. (1969), and dolomite,

$$1000 \ln \alpha^{o}_{\text{dolomite-water}} = \{[2.62(10^6)]/T^2\} + 2.17, \quad (7)$$

from Fritz and Smith (1970). Assuming that carbonate precipitation occurred at 276.85 K (3.7°C) and 293.75 K (20.6°C), equivalent to depths at the seafloor and 300 mbsf at Site 1251 (Tréhu, Bohrmann, Rack, Torres, et al., 2003), the estimated isotopic fractionations are +32.9‰ (SMOW) at 3.7°C and +28.8‰ at 20.6°C for calcite and +36.4‰ and +32.5‰ for dolomite, respectively. The precipitation of carbonates accounts for the observed decreases in $\delta^{18}O$ of interstitial water at all sites (Fig. **F2C**). Thus, the predicted greater decrease in $\delta^{18}O$ (~5‰) in the slope basin, compared to that at the summit and flank sites (~0.3‰) as mentioned above, likely reflects abundant authigenic carbonate and possibly high dolomite content and/or low precipitation temperature. Alternatively, Sr^{2+} concentration and the strontium isotopic composition ($^{87}Sr/^{86}Sr$) of interstitial waters measured in these fluids suggest the influence of fluid interaction with oceanic basement (Torres et al., 2004b; Teichert et al., 2005). The $\delta^{18}O$ values of oceanic basement recovered from the eastern flank of Juan de Fuca Ridge during ODP Leg 168 range from +6.1‰ to +19.3‰ (Vienna SMOW), showing a positive correlation between $\delta^{18}O$ and the percentage of bulk rock alteration (Hunter et al., 1999). Oceanic basement in contact with seawater preferentially incorporates ^{18}O into its alteration products, resulting in a significant decrease of $\delta^{18}O$ of interstitial waters. The effect of basalt alteration in deep fluids at Hydrate Ridge shows an increase eastward (landward) (Torres et al., 2004b), consistent with the observed greater decrease in $\delta^{18}O$ in the eastern slope basin of the ridge relative to the summit and flank regions.

CONCLUSIONS

Occurrence of subsurface gas hydrates is well documented by anomalies of δD, $\delta^{18}O$, and Cl^- of interstitial waters. Positive anomalies of δD and $\delta^{18}O$ correlating with low Cl^- concentrations are seen in gas hydrate bearing-sediments because of the dissociation of gas hydrate during core retrieval. On the other hand, negative anomalies of δD and $\delta^{18}O$ correlating with high Cl^- concentrations are observed in the vicinity of actively forming massive gas hydrates on the crest of Hydrate Ridge. These anomalies are due to the fact that residual waters have not been diffused away because of gas hydrate development, in contrast to all data from hydrate sites published in the literature.

The shallow interstitial waters (<40 mbsf) at all sites show slight increases in Cl^-, δD, and $\delta^{18}O$, which record the geochemical change of seawater composition due to the fresh and isotopically light water stored in ice sheets during the LGM. However, observed Cl^- concentration, δD, and $\delta^{18}O$ values deeper than several tens of meters below the seafloor are the combined result of clay mineral dehydration, carbonate precipitation, and alteration of oceanic basement. The observed freshening in Cl^- and depletion in D in the eastern slope basin, caused by the dehydration of clay minerals beneath the accreted mélange, can be used to document the progressive contribution of water from clay minerals from deeper and older sediments landward of the toe of the accretionary prism. Downward decreases in $\delta^{18}O$ are observed over the ridge, probably caused by the carbonate precipitation and basalt alteration. The relatively large effects of the dehydration and the basalt alteration in the eastern slope basin of the ridge reflect progressive landward diagenesis due to the eastward subduction.

ACKNOWLEDGMENTS

This research used samples and/or data provided by the Ocean Drilling Program (ODP). ODP is sponsored by the U.S. National Science Foundation (NSF) and participating countries under management of Joint Oceanographic Institutions (JOI), Inc. We thank the captain and crew of the *JOIDES Resolution* and the ODP technical staff for this successful cruise. We also express our thanks to D. Graham and B. Jones for their great assistance in the chemistry laboratory. We acknowledge helpful reviews by G. Dickens and R. Hesse. Funding for this research was provided in part by a grant-in-aid from the Japan Ministry of Education, Culture, Sports, Science and Technology and in part by a grant from the Japan Petroleum Exploration Company (JAPEX) to Ryo Matsumoto while the first author was at the University of Tokyo.

REFERENCES

Adkins, J.F., McIntyre, K., and Schrag, D.P., 2002. The salinity, temperature and $\delta^{18}O$ of the glacial deep ocean. *Science,* 298:1769–1773. doi:10.1126/science.1076252

Bekins, B., McCaffrey, A.M., and Driess, S.J., 1994. Influence of kinetics on the smectite to illite transition in the Barbados accretionary prism. *J. Geophys. Res.,* 99:18147–18158. doi:10.1029/94JB01187

Borowski, W.S., Paull, C.K., and Ussler, III, W., 1996. Marine pore-water sulfate profiles indicate in situ methane flux from underlying gas hydrate. *Geology,* 24(7):655–658. doi:10.1130/0091-7613(1996)024<0655:MPWSPI>2.3.CO;2

Capuano, R.M., 1992. The temperature dependence of hydrogen isotope fractionation between clay minerals and water; evidence from a geopressured system. *Geochim. Cosmochim. Acta,* 56:2547–2554. doi:10.1016/0016-7037(92)90208-Z

Coleman, D.D., Risatti, J.B., and Schoell, M., 1981. Fractionation of carbon and hydrogen isotopes by methane-oxidising bacteria. *Geochim. Cosmochim. Acta,* 45:1033–1037. doi:10.1016/0016-7037(81)90129-0

Coplen, T.B., and Hanshaw, B.D., 1973. Ultrafiltration by a compacted clay membrane, I. Oxygen and hydrogen isotopic fractionation. *Geochim. Cosmochim. Acta,* 37:2295–2310. doi:10.1016/0016-7037(73)90105-1

Dählmann, A., and de Lange, G.J., 2003. Fluid-sediment interactions at eastern Mediterranean mud volcanos: a stable isotope study from ODP Leg 160. *Earth Planet. Sci. Lett.,* 212:377–391. doi:10.1016/S0012-821X(03)00227-9

Egeberg, P.K., and Dickens, G.R., 1999. Thermodynamic and pore water halogen constraints on gas hydrate distribution at ODP Site 997 (Blake Ridge). *Chem. Geol.,* 153:53–79. doi:10.1016/S0009-2541(98)00152-1

Epstein, S., and Mayeda, T., 1953. Variation of ^{18}O content of waters from natural sources. *Geochim. Cosmochim. Acta,* 4:213–224. doi:10.1016/0016-7037(53)90051-9

Fritz, P., and Smith, D.G.W., 1970. The isotopic composition of secondary dolomites. *Geochim. Cosmochim. Acta.,* 34:1161–1173. doi:10.1016/0016-7037(70)90056-6

Gehre, M., Hoefling, R., Kowski, P., and Strauch, G., 1996. Sample preparation device for quantitative hydrogen isotope analysis using chromium metal. *Anal. Chem.,* 68:4414–4417. doi:10.1021/ac9606766

Goldfinger, C., Kulm, L.D., Yeats, R.S., McNeill, L., and Hummon, C., 1997. Oblique strike-slip faulting of the central Cascadia submarine forearc. *J. Geophys. Res.,* 102:8217–8244. doi:10.1029/96JB02655

Hanor, J.S., 1987. Origin and migration of subsurface sedimentary brines. *SEPM Short Course,* 21.—*Soc. Econ. Paleontol. Mineral.*

Heeschen, K.U., Tréhu, A.M., Collier, R.W., Suess, E., and Rehder, G., 2003. Distribution and height of methane bubble plumes on the Cascadia margin characterized by acoustic imaging. *Geophys. Res. Lett.,* 30:1643–1646. doi:10.1029/2003GL016974

Hesse R., 2003. Pore water anomalies of submarine gas-hydrate zones as tool to assess hydrate abundance and distribution in the subsurface—what have we learned in the past decade? *Earth-Sci. Rev.,* 61:149–179. doi:10.1016/S0012-8252(02)00117-4

Hesse, R., Frape, S.K., Egeberg, P.K., and Matsumoto, R., 2000. Stable isotope studies (CI, O, and H) of interstitial waters from Site 997, Blake Ridge gas hydrate field, West Atlantic. *In* Paull, C.K., Matsumoto, R., Wallace, P.J., and Dillon, W.P. (Eds.), *Proc. ODP, Sci. Results,* 164: College Station, TX (Ocean Drilling Program), 129–137. [HTML]

Hunter, A.G., Kempton, P.D., and Greenwood, P., 1999. Low-temperature fluid-rock interaction: an isotopic and mineralogical perspective of upper crustal evolution, eastern flank of the Juan de Fuca Ridge (JdFR), ODP Leg 168. *Chem. Geol.,* 155:3–28. doi:10.1016/S0009-2541(98)00138-7

Kastner, M., and Elderfield, H., 1995. Data report: Chemical and isotopic compositions of pore fluids in sediments of the Cascadia accretionary complex. *In* Carson, B., Westbrook, G.K., Musgrave, R.J., and Suess, E. (Eds.), *Proc. ODP, Sci. Results,* 146 (Pt 1): College Station, TX (Ocean Drilling Program), 431–438.

Kharaka, Y.K., and Berry, F.A.P., 1973. Simultaneous flow of water and solute through geological membranes. I: experimental investigations. *Geochim. Cosmochim. Acta,* 37:2577–2603. **doi:10.1016/0016-7037(73)90267-6**

MacKay, M.E., 1995. Structural variation and landward vergence at the toe of the Oregon accretionary prism. *Tectonics,* 14:1309–1320. **doi:10.1029/95TC02320**

MacKay, M.E., Moore, G.F., Cochrane, G.R., Moore, J.C., and Kulm, L.D., 1992. Landward vergence and oblique structural trends in the Oregon margin accretionary prism: implications and effect on fluid flow. *Earth Planet. Sci. Lett.,* 109:477–491. **doi:10.1016/0012-821X(92)90108-8**

Matsumoto, R., and Borowski, W.S., 2000. Gas hydrate estimates from newly determined oxygen isotopic fractionation ($\alpha_{GH\text{-}IW}$) and $\delta^{18}O$ anomalies of the interstitial waters: Leg 164, Blake Ridge. *In* Paull, C.K., Matsumoto, R., Wallace, P.J., and Dillon, W.P. (Eds.), *Proc. ODP, Sci. Results,* 164: College Station, TX (Ocean Drilling Program), 59–66. [**HTML**]

McDuff, R.E., 1985. The chemistry of interstitial waters, Deep Sea Drilling Project Leg 86. *In* Heath, G.R., Burckle, L.H., et al., *Init. Repts. DSDP,* 86: Washington (U.S. Govt. Printing Office), 675–687.

Milkov, A.V., Claypool, G.E., Lee, Y-J., Xu, W., Dickens, G.R., Borowski, W.S., and the ODP Leg 204 Scientific Party, 2003. In situ methane concentrations at Hydrate Ridge offshore Oregon: new constraints on the global gas hydrate inventory from an active margin. *Geology,* 31:833–836.

Milkov, A.V., Dickens, G.R., Claypool, G.E., Lee, Y-J., Borowski, W.S., Torres, M.E., Xu, W., Tomaru, H., Tréhu, A.M., and Schultheiss, P., 2004. Co-existence of gas hydrate, free gas, and brine within the regional gas hydrate stability zone at Hydrate Ridge (Oregon margin): evidence from prolonged degassing of a pressurized core. *Earth Planet. Sci. Lett.,*222:829–843. **doi:10.1016/j.epsl.2004.03.028**

O'Neil, J.R., 1968. Hydrogen and oxygen isotope fractionation between ice and water. *J. Phys. Chem.,* 72:3683–3684. **doi:10.1021/j100856a060**

O'Neil, J.R., Clayton, R.N., and Mayeda, T.K., 1969. Oxygen isotope fractionation in divalent metal carbonates. *J. Chem. Phys.,* 51:5547–5558.

Perry, E., and Hower, J., 1970. Burial diagenesis in Gulf Coast pelitic sediments. *Clays Clay Miner.,* 18:165–177.

Pytte, A.M., and Reynolds, R.C., 1989. The thermal transformation of smectite to illite. *In* Naeser, N.D., and McCulloh, T.H. (Eds.), *Thermal History of Sedimentary Basins: Methods and Case Histories:* New York (Springer), 133–140.

Savin, S.M., and Lee, M., 1988. Isotopic studies of phyllosilicates. *In* Bailey, S.W. (Ed.), *Hydrous Phyllosilicates (Exclusive of Micas).* Min. Soc. Am., Rev. Mineral., 19:189–223.

Schrag, D.P., Hampt, G., and Murray, D.W., 1996. Pore fluid constraints on the temperature and oxygen isotopic composition of the glacial ocean. *Science,* 272:1930–1932.

Suess, E.M., Torres, M.E., Bohrmann, G., Collier, R.W., Greinter, J., Linke, P., Rehter, G., Tréhu, A.M., Wallmann, K., Winckler, G., and Zulegger, E., 1999. Gas hydrate destabilization: enhanced dewatering, benthic material turnover, and large methane plumes at the Cascadia convergent margin. *Earth Planet. Sci. Lett.,* 170:1–15. **doi:10.1016/S0012-821X(99)00092-8**

Teichert, B.M.A., Torres, M.E., Bohrmann, G., and Eisenhauer, A., 2005. Fluid sources, fluid pathways and diagenetic reactions across an accretionary prism revealed by Sr and B geochemistry. *Earth Planet. Sci. Lett.,* 239:106–121. **doi:10.1016/j.epsl.2005.08.002**

Torres, M.E., McManus, J., Hammond, D.E., de Angelis, M.A., Heeschen, K.U., Colbert, S.L., Tryon, M.D., Brown, K.M., and Suess, E., 2002. Fluid and chemical fluxes in and out of sediments hosting methane hydrate deposits on Hydrate Ridge. *Earth Planet. Sci. Lett.,* 201:525–540. **doi:10.1016/S0012-821X(02)00733-1**

Torres, M.E., Wallmann, K., Tréhu, A.M., Bohrmann, G., Borowski, W.S., and Tomaru, H., 2004a. Gas hydrate growth, methane transport, and chloride enrichment at the southern summit of Hydrate Ridge, Cascadia margin off Oregon. *Earth Planet. Sci. Lett.,* 226:225–241. **doi:10.1016/j.epsl.2004.07.029**

Torres, M.E., Teichert, B.M.A., Tréhu, A.M., Borowski, W.S., and Tomaru, H., 2004b. Relationship of pore water freshening to accretionary processes in the Cascadia margin: fluid sources and gas hydrate abundance. *Geophys. Res. Lett.,* 31:L22305. **doi:10.1029/2004GL021219**

Tréhu, A.M., Bohrmann, G., Rack, F.R., Torres, M.E., et al., 2003. *Proc. ODP, Init. Repts.,* 204 [Online]. Available from World Wide Web: <**http://www-odp.tamu.edu/publications/204_IR/204ir.htm**>.

Tréhu, A.M., Bohrmann, G., Rack, F.R., Collett, T.S., Goldberg, D.S., Long, P.E., Milkov, A.V., Riedel, M., Schultheiss, P., Torres, M.E., Bangs, N.L., Barr, S.R., Borowski, W.S., Claypool, G.E., Delwiche, M.E., Dickens, G.R., Gracia, E., Guerin, G., Holland, M., Johnson, J.E., Lee, Y.-J., Liu, C.-S., Su, X., Teichert, B., Tomaru, H., Vanneste, M., Watanabe, M., and Weinberger, J.L., 2004. Three-dimensional distribution of gas hydrate beneath southern Hydrate Ridge: constraints from ODP Leg 204. *Earth Planet. Sci. Lett.,* 222(3–4):845–862. **doi:10.1016/j.epsl.2004.03.035**

Waseda, A., and Uchida, T., 2002. Origin of methane in natural gas hydrates from the Mackenzie Delta and Nankai Trough. *Proc. 4th Int. Conf. Gas Hydrates*, Yokohama, 169–174.

Figure F1. A. Location and geological setting of Hydrate Ridge. Juan de Fuca plate is obliquely subducting beneath North American plate ~20 km west of the ridge. Box denotes area of the detailed bathymetric map. **B.** Detailed bathymetric map of the southern Hydrate Ridge and drilling sites of Leg 204. From Tréhu, Bohrmann, Rack, Torres, et al. (2003).

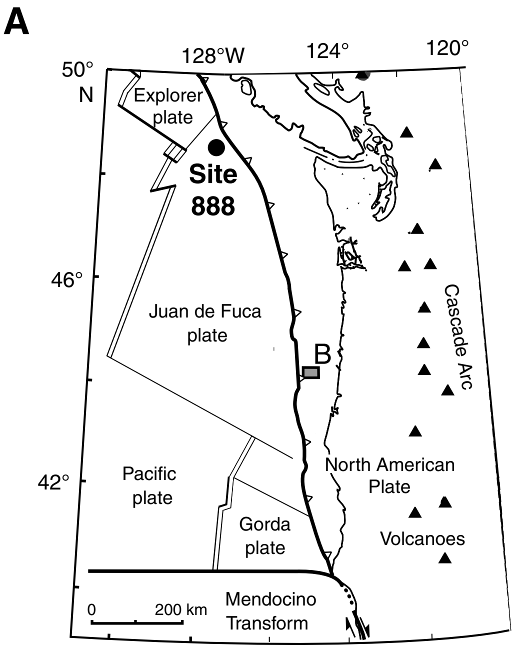

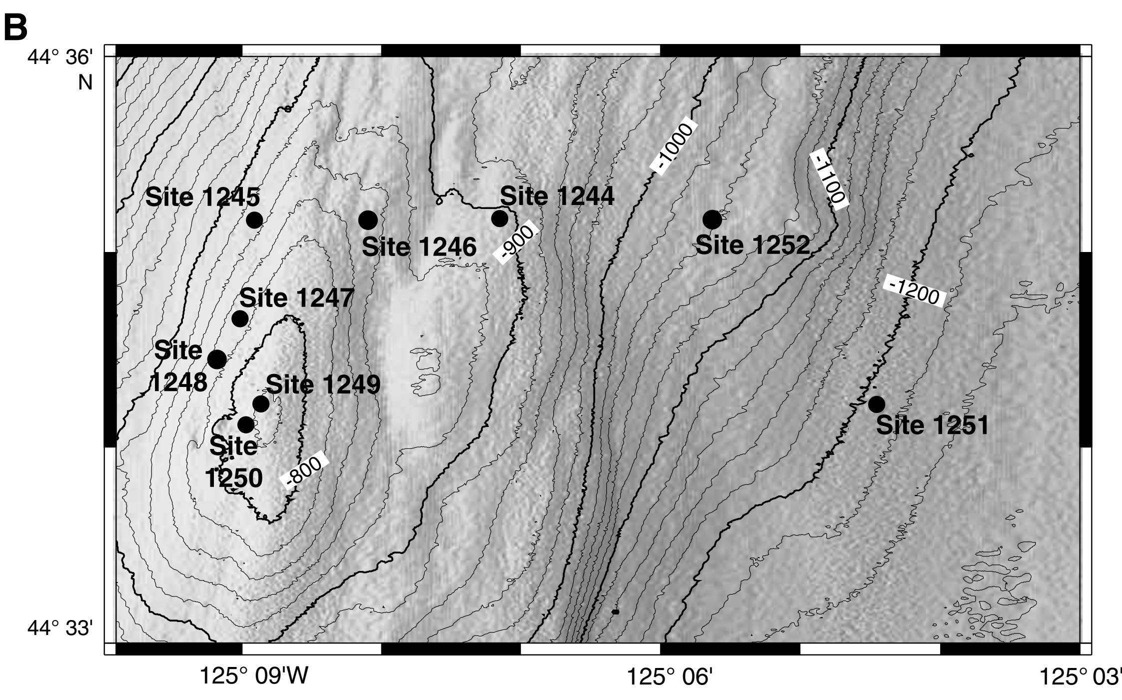

Figure F2. A. Dissolved Cl^- concentrations of interstitial waters from ODP Legs 204 and 146 (Site 888; data from Kastner and Elderfields, 1995). Note different scale for ridge summit. (Continued on next two pages.)

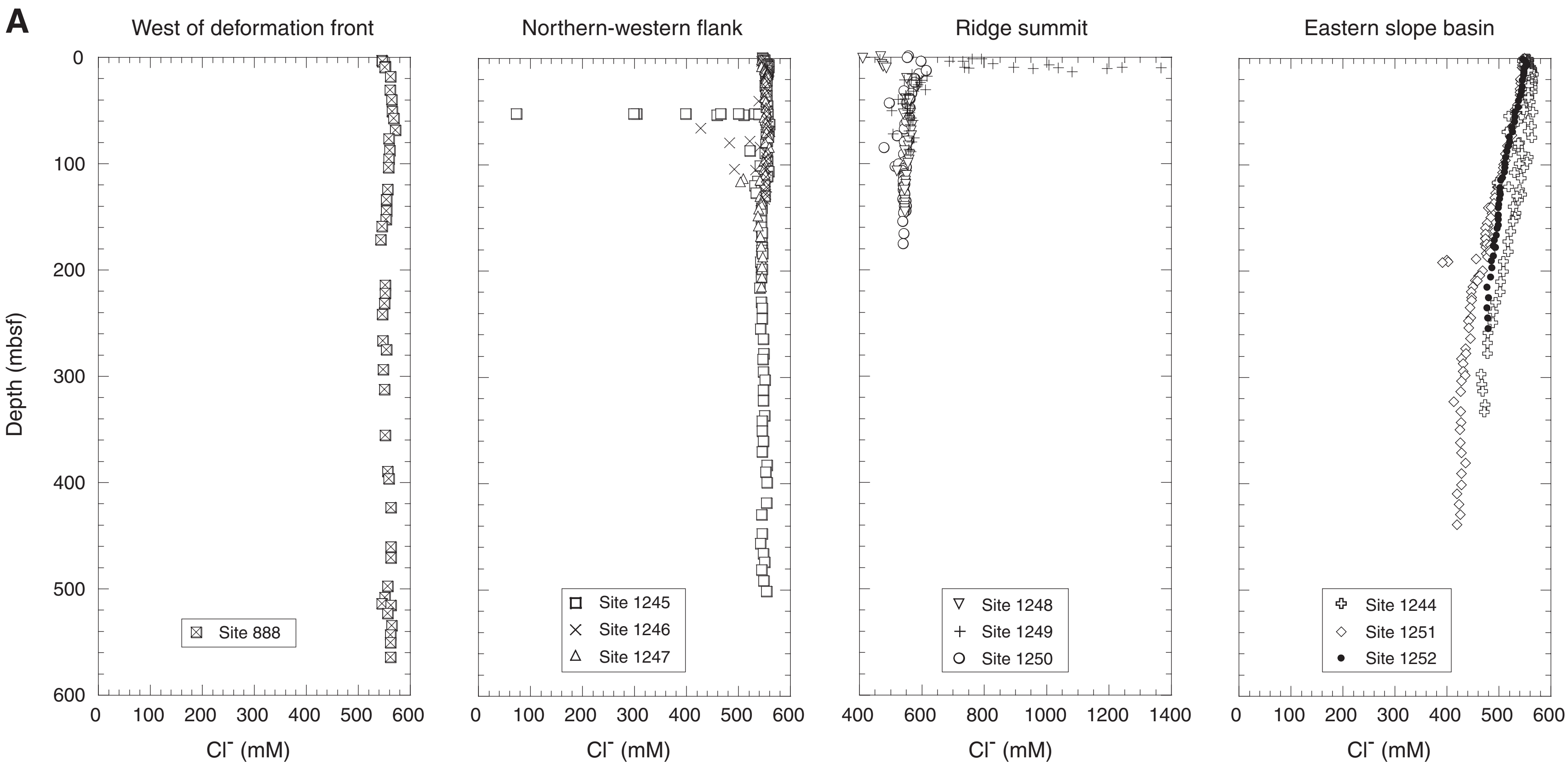

Figure F2 (continued). B. δD values of interstitial waters from Leg 204. SMOW = Standard Mean Ocean Water.

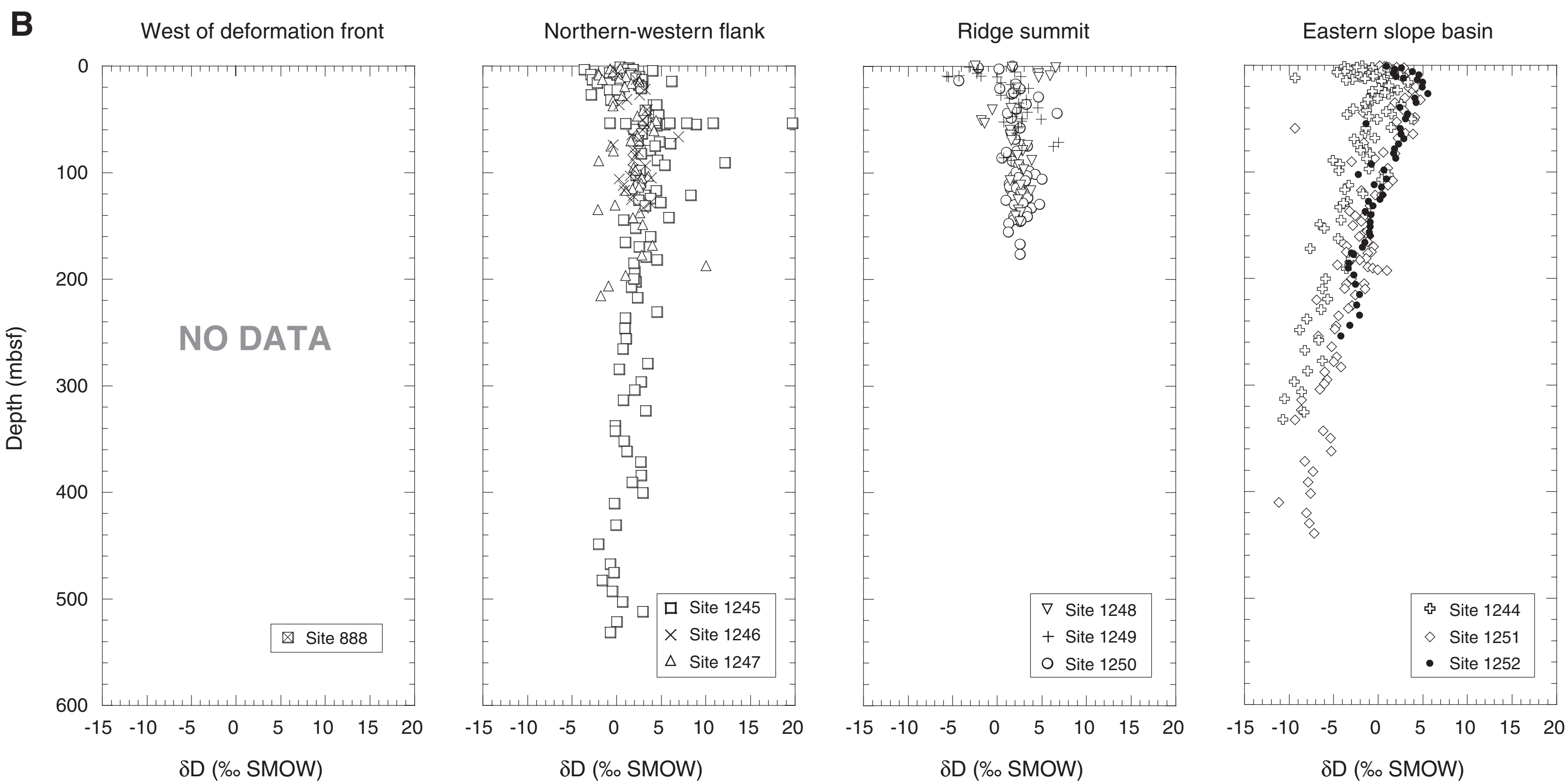

Figure F2 (continued). C. δ^{18}O values of interstitial waters from Legs 204 and 146 (Site 888; data from Kastner and Elderfields, 1995).

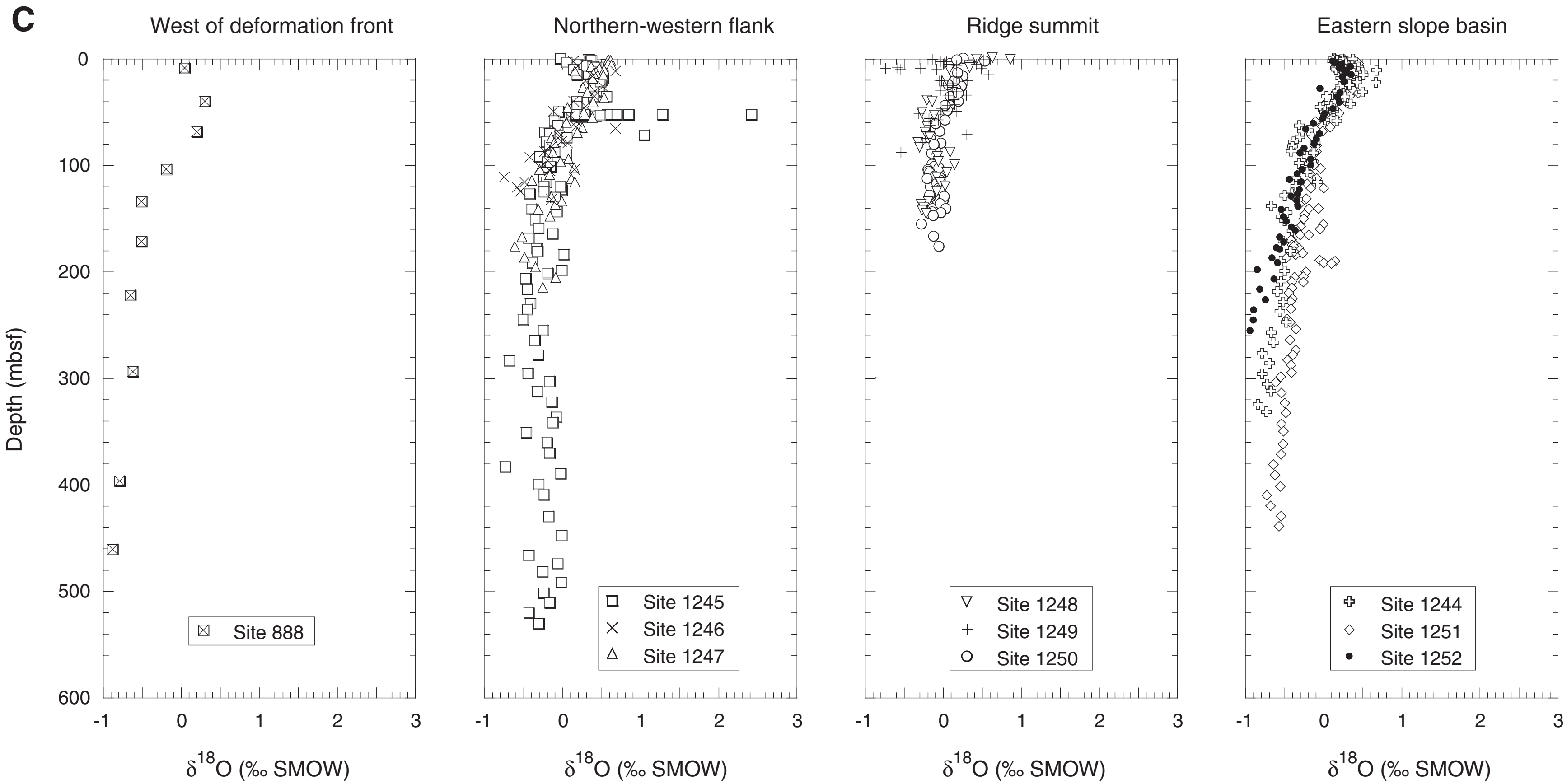

Figure F3. Discrete Cl⁻ excursions within the GHSZ correlate well with other proxies of gas hydrate abundance, such as temperature anomalies in the cores (temperature distribution for Holes 1244C and 1251D; temperature deviation for Hole 1245B), as shown by Tréhu et al. (2004). Here we show that the isotopic composition of the water shows deviations to high δD and $\delta^{18}O$ values. These anomalies reflect release of water enriched in the heavy isotopes as the gas hydrate is destabilized during core retrieval (Cl^- and temperature anomaly profiles are modified from Tréhu et al., 2004). BSR = bottom-simulating reflector, APC = advanced piston corer, XCB = extended core barrel, T = temperature. SMOW = Standard Mean Ocean Water.

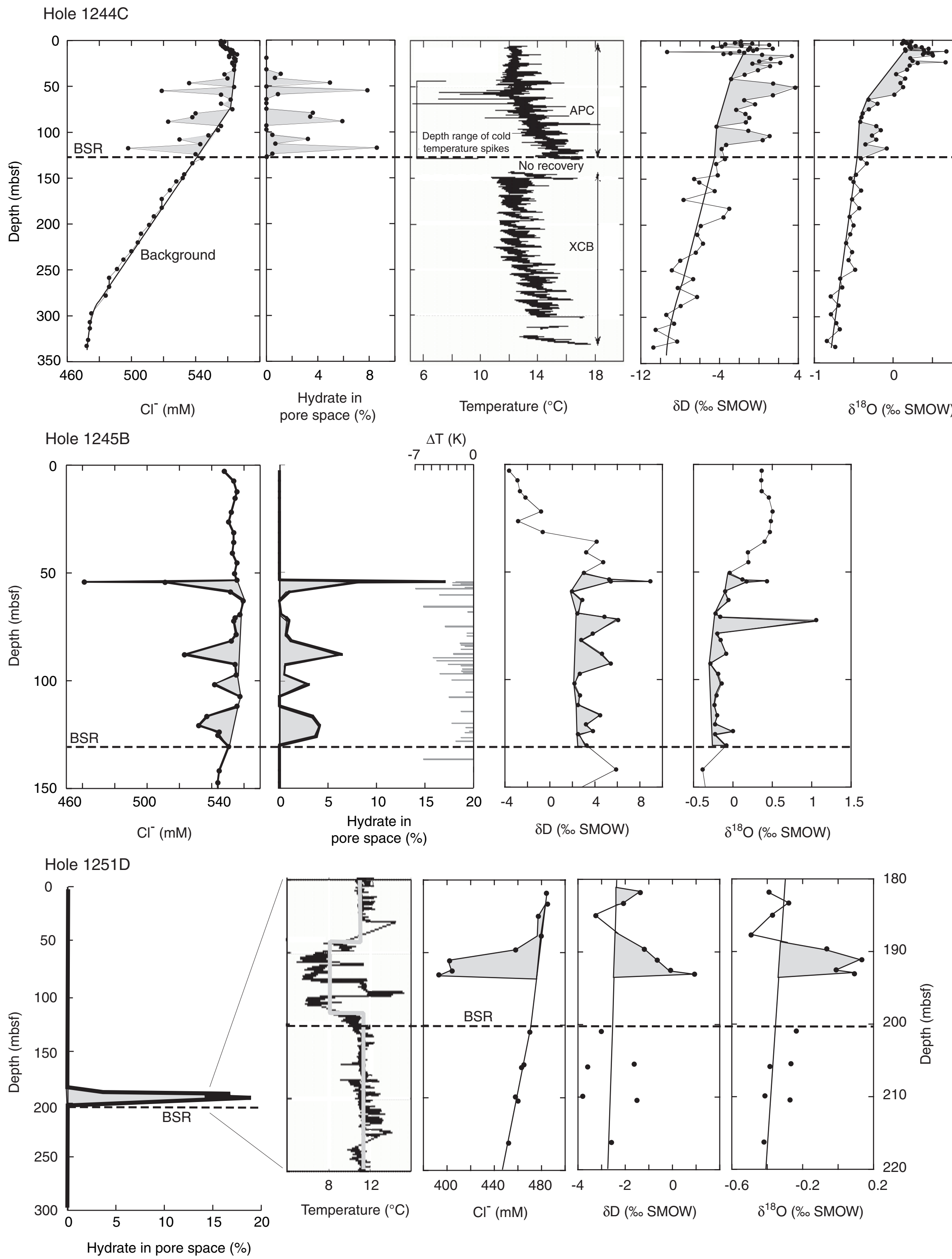

Figure F4. (**A**) Cl^- concentrations and (**B**) δD and (**C**) $\delta^{18}O$ values in the eastern slope basin of Hydrate Ridge. Boxes denote increases of Cl^-, δD, and $\delta^{18}O$ within Holocene and Pleistocene sediments caused by ice sheet development during the Last Glacial Maximum. Dashed lines in B indicate best-fit average temperatures/depths of hydrogen isotopic fractionation between clay and water, which are increasing eastward. Dashed lines in C indicate predicted background levels of $\delta^{18}O$ after correction for clay mineral dehydration. SMOW = Standard Mean Ocean Water.

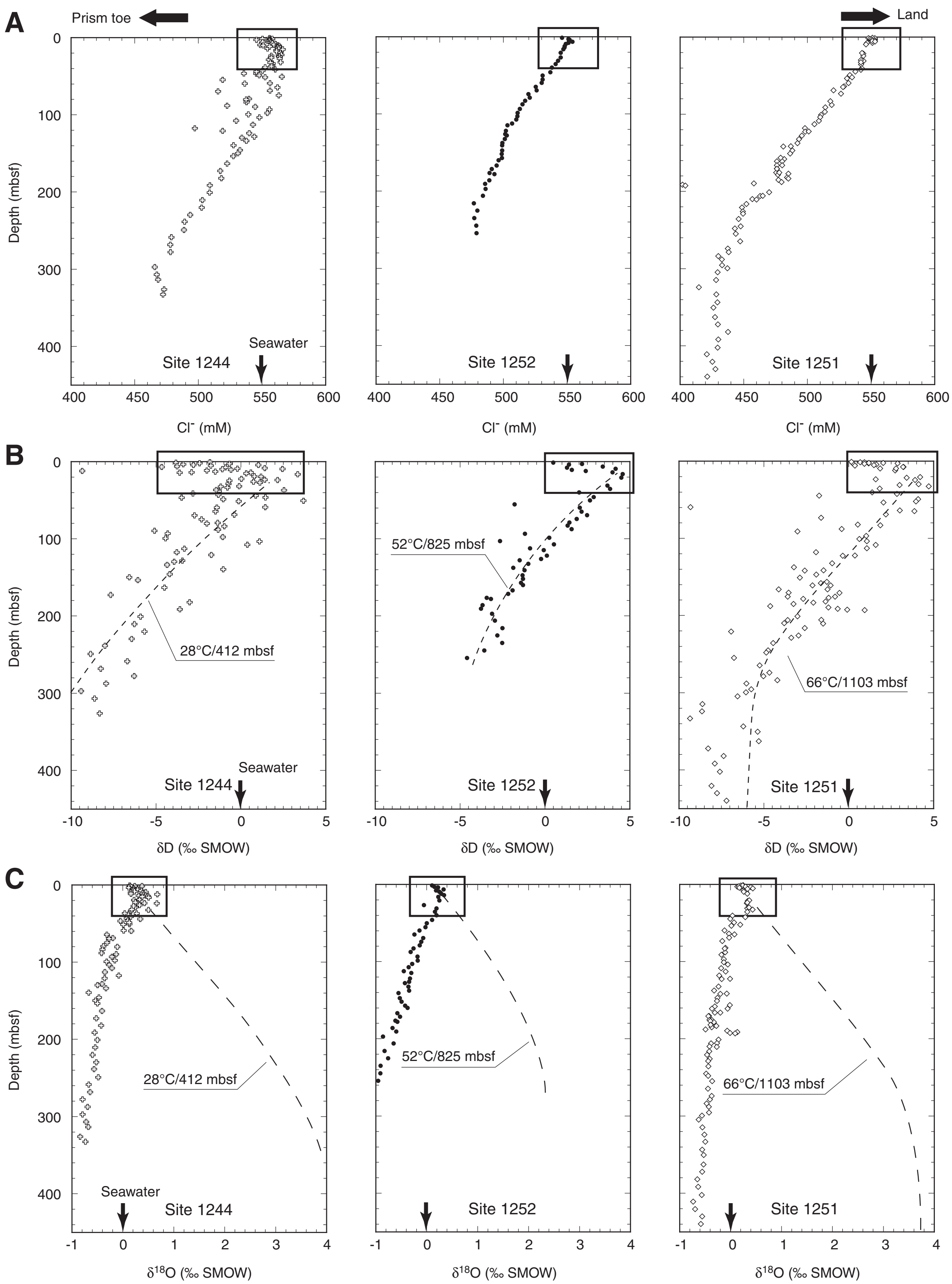

Table T1. Hydrogen and oxygen isotopic compositions of interstitial waters, Sites 1244–1252. (See table note. Continued on next two pages.)

Core, section, interval (cm)	Depth (mbsf)	δD (‰)	$\delta^{18}O$ (‰)
204-1244B-			
1H-1, 140–150	1.40	–3.8	0.38
1H-3, 140–150	4.40	–2.8	0.27
2H-2, 140–150	9.50	2.5	0.18
2H-5, 140–150	14.00	0.6	0.31
3H-2, 140–150	19.00	0.8	0.33
3H-5, 140–150	23.50	1.4	0.43
4H-3, 135–150	28.63	–0.7	0.25
4H-7, 22–32	33.50	–0.8	0.16
5H-3, 135–150	38.46	–1.3	0.11
5H-6, 129–150	42.90	–1.3	0.08
6H-3, 135–150	46.78	–3.5	–0.05
6H-6, 135–150	51.28	–0.1	0.01
204-1244C-			
1H-1, 65–75	0.65	–1.8	0.13
1H-1, 65–75	1.40		0.23
1H-2, 65–75	2.15	–2.4	0.14
1H-2, 140–150	2.90	–0.7	0.17
1H-3, 65–75	3.65	–3.4	0.12
1H-3, 140–150	4.40	1.0	0.21
1H-4, 60–70	5.10	–1.8	0.21
2H-1, 66–75	6.15	–3.8	0.29
2H-1, 140–175	6.90	–4.7	0.21
2H-2, 66–75	7.65	–0.9	0.36
2H-2, 140–175	8.40	1.4	0.23
2H-3, 66–75	9.15	–0.2	0.45
2H-3, 140–175	9.90	–1.1	0.15
2H-4, 66–75	10.65	–0.6	0.39
2H-4, 140–175	11.40	–2.0	0.16
2H-5, 66–75	12.15	–9.3	0.68
2H-5, 140–175	12.90	–1.5	0.40
2H-6, 66–75	13.65	–2.9	0.45
2H-6, 140–175	14.40	–3.6	0.50
2H-7, 64–74	15.14	0.3	0.38
3H-1, 140–150	16.40	3.3	0.51
3H-3, 140–150	19.40	1.2	0.22
3H-5, 140–150	22.40	0.0	0.25
3H-6, 140–150	23.90	2.2	0.67
3H-7, 140–150	24.84	–0.7	0.31
4H-2, 140–150	27.35	1.1	0.21
4H-5, 140–150	31.85	–0.1	0.18
5H-2, 140–150	36.85	–1.5	0.04
5H-5, 140–150	41.35	–2.8	0.15
6H-2, 140–150	46.35	1.4	0.10
6H-5, 140–150	50.71	3.7	0.13
7H-5, 140–150	58.97	1.4	0.02
8H-2, 140–150	64.37	–1.5	–0.31
8H-5, 140–150	68.87	–0.4	–0.20
9H-2, 140–150	74.85	–2.3	–0.31
9H-5, 140–150	79.35	–1.4	–0.38
10H-2, 140–150	83.55	–1.0	–0.40
10H-5, 140–150	88.38	–1.3	–0.42
11H-2, 140–150	93.08	–4.3	–0.21
11H-5, 140–150	97.58	–1.1	–0.15
12H-2, 140–150	103.35	1.1	–0.27
12H-5, 140–150	107.85	0.4	–0.21
13H-2, 140–150	112.85	–3.3	–0.35
13H-5, 140–150	117.35	–3.8	–0.08
15H-5, 140–150	128.35	–3.4	–0.41
17H-2, 140–150	133.70	–4.3	–0.33
19X-2, 140–150	145.85	–4.2	–0.47
19X-5, 140–150	149.85	–6.6	–0.54
20X-3, 140–150	153.55	–6.1	–0.50
21X-3, 140–150	163.15	–4.5	–0.41
22X-3, 140–150	172.65	–7.7	–0.52
23X-3, 140–150	182.25	–3.0	–0.43
24X-3, 140–150	191.45	–3.6	–0.55
25X-3, 140–150	200.75	–5.9	–0.50
26X-3, 140–150	210.45	–6.3	–0.54
27X-3, 140–150	220.10	–5.7	–0.60
28X-3, 140–150	229.70	–6.4	–0.52
29X-3, 140–150	238.56	–8.0	–0.56
30X-3, 140–150	249.00	–8.9	–0.48
31X-3, 140–150	258.60	–6.7	–0.67
32X-3, 140–150	268.24	–8.3	–0.64
33X-3, 140–150	277.84	–6.3	–0.79
34X-3, 140–150	287.60	–7.9	–0.69
35X-3, 140–150	297.33	–9.4	–0.79
36X-3, 140–150	306.90	–8.6	–0.72
37X-1, 140–150	313.50	–10.5	–0.68
38X-3, 140–150	326.20	–8.3	–0.84
39X-1, 140–150	332.80	–10.7	–0.73
204-1244E-			
4H-5, 0–20	26.20	0.7	0.33
5H-2, 135–150	32.50	–1.2	0.50
5H-5, 135–150	37.00	2.5	0.27
7H-2, 135–150	44.05	0.9	0.34
7H-5, 135–150	48.55	–1.0	0.12
9H-5, 135–150	59.51	–1.4	0.17
10H-6, 0–20	69.60	–2.7	–0.27
12H-5, 135–150	80.05	–2.0	–0.11
13H-5, 135–150	89.75	–5.1	–0.13
14H-5, 125–140	99.37	–4.4	–0.32
17H-5, 135–150	120.95	–1.7	–0.36
18H-5, 135–150	129.70	–3.9	–0.50
19H-5, 135–150	139.55	–1.0	–0.67
204-1245B-			
1H-2, 140–150	2.90	–3.6	0.36
1H-5, 140–150	7.40	–2.9	0.36
2H-2, 140–150	12.40	–2.7	0.36
2H-4, 140–150	15.40	–2.2	0.46
3H-2, 140–150	21.90	–0.8	0.50
3H-5, 140–150	26.40	–2.8	0.48
4H-2, 140–150	31.40	–0.6	0.47
4H-5, 140–150	35.90	4.1	0.40
5H-2, 140–150	40.90	3.2	0.19
5H-5, 140–150	45.40	4.7	0.19
6H-2, 140–150	50.40	3.0	–0.04
6H-4, 140–150	53.40	5.3	0.12
6H-5, 78–88	54.28	8.9	0.43
6H-5, 88–103	54.38	5.4	0.17
7H-2, 140–150	58.95	2.0	–0.10
7H-5, 140–150	62.98	2.9	–0.06
8H-2, 132–142	69.32	2.4	–0.22
8H-3, 140–150	70.82	4.8	–0.16
8H-4, 140–150	72.32	6.1	1.06
9H-2, 134–144	78.66	3.8	–0.20
9H-4, 140–150	81.62	2.8	–0.15
10H-2, 103–113	88.03	4.6	–0.09
10H-5, 140–150	92.53	5.4	–0.29
11H-2, 140–150	97.37	2.7	–0.19
11H-5, 140–150	101.87	2.2	–0.14
12H-2, 140–150	107.37	2.7	–0.21
12H-5, 140–150	111.87	2.5	–0.23
13H-2, 111–126	116.61	4.5	–0.20
13H-5, 104–119	120.80	3.2	–0.23
14H-1, 125–140	123.95	3.8	0.00
14H-2, 135–150	125.45	2.5	–0.23
15X-3, 130–150	130.66	3.2	–0.08
16X-3, 130–150	141.80	5.9	–0.38
18X-2, 113–138	151.73	2.2	–0.34
19X-2, 125–150	159.75	3.8	–0.30
20X-2, 125–150	169.25	2.6	–0.42
21X-2, 117–142	178.77	3.3	–0.32
21X-4, 77–102	181.27	4.6	–0.31
22X-5, 125–150	192.65	2.1	–0.38
23X-5, 125–150	201.95	2.2	–0.18
24X-2, 125–150	206.95	1.7	–0.46
25X-2, 125–150	216.74	2.4	–0.44
26X-5, 75–100	230.33	4.6	–0.41
27X-2, 125–150	236.05	1.0	–0.44
28X-2, 125–150	245.68	1.0	–0.50
29X-2, 125–150	255.35	1.1	–0.24
30X-2, 125–150	264.95	0.7	–0.35
31X-5, 125–150	278.76	3.5	–0.31
32X-2, 125–150	284.25	0.3	–0.68
34X-2, 125–150	295.95	2.8	–0.44
35X-2, 125–150	303.55	2.1	–0.16
36X-2, 125–150	313.15	0.8	–0.32
37X-2, 125–150	322.75	3.3	–0.13
38X-5, 125–150	336.95	–0.2	–0.07
39X-2, 125–150	341.95	–0.1	–0.11
40X-2, 125–150	351.65	0.9	–0.46
41X-2, 125–150	361.25	1.2	–0.19
42X-2, 125–150	370.95	2.7	–0.16
43X-4, 125–150	383.55	2.8	–0.73
44X-2, 125–150	390.15	1.8	–0.01
45X-2, 125–150	399.85	3.0	–0.30
47X-2, 125–150	409.80	–0.2	–0.23
49X-4, 0–25	430.11	0.0	–0.17
51X-2, 125–150	447.95	–2.0	–0.01
53X-2, 125–150	466.75	–0.7	–0.43
204-1245C-			
2H-5, 140–150	14.90	2.9	0.34
4H-5, 140–150	26.40	0.3	0.40
5H-5, 140–150	35.90	4.5	0.57
7H-5, 32–34	53.12	4.1	0.18
7H-5, 35–37	53.15	4.4	0.58
7H-5, 37–39	53.17	6.0	0.70
7H-5, 41–43	53.21	10.8	1.29
7H-5, 42–44	53.22	19.7	2.43
7H-5, 44–46	53.24	7.9	0.85
7H-5, 47–49	53.27	–0.7	0.29
7H-5, 50–52	53.30	1.1	0.49
7H-6, 98–108	55.28	4.5	0.25
10H-6, 0–30	74.48	4.3	0.06
12H-2, 125–140	90.25	12.2	0.05
15X-4, 130–150	120.62	8.3	–0.01
17X-4, 110–130	127.35	5.0	–0.41
20X-4, 75–100	143.95	0.8	–0.07
22X-5, 125–150	165.15	1.0	–0.12
24H-5, 125–150	184.35	2.0	0.03
28H-2, 80–100	199.20	1.9	0.00
204-1245D-			
1H-1, 60–70	0.60	0.4	–0.02
1H-1, 135–150	1.35	1.4	0.35
1H-2, 65–75	2.15	1.3	0.38
1H-2, 135–150	2.85	1.8	0.23
1H-3, 85–100	3.85	4.0	0.06
1H-3, 135–150	4.35	3.1	0.35
2H-1, 65–75	5.65	–0.8	0.57
2H-1, 135–150	6.35	0.8	0.20
2H-2, 65–75	7.15	1.6	0.31
2H-2, 135–150	7.85	0.1	0.40
2H-3, 65–75	8.65	1.7	0.51
2H-3, 135–150	9.35	2.6	0.44
2H-4, 135–150	10.85	2.2	0.14
2H-5, 135–150	12.35	2.9	0.47
2H-6, 135–150	13.85	6.2	0.52
3H-1, 135–150	15.85	0.4	0.19
3H-2, 135–150	17.35	2.5	0.52
3H-3, 135–150	18.85	2.8	0.53
3H-4, 135–150	20.35	2.8	0.51
3H-5, 135–150	21.85	0.1	0.49

Table T1 (continued).

Core, section, interval (cm)	Depth (mbsf)	δD (‰)	$\delta^{18}O$ (‰)
204-1245E-			
1R-1, 120–135	474.90	–0.3	–0.06
2R-1, 69–89	482.29	–1.6	–0.25
3R-1, 114–144	492.34	–0.4	–0.01
4R-1, 130–150	502.20	0.7	–0.23
5R-1, 122–144	511.72	3.0	–0.16
6R-1, 85–105	521.05	0.0	–0.42
7R-1, 132–150	531.12	–0.7	–0.29
204-1246B-			
1H-2, 145–150	2.95	–0.2	0.14
2H-2, 145–160	7.65	0.0	0.20
2H-5, 145–150	12.15	2.2	0.69
3H-2, 140–150	17.10	2.5	0.39
3H-5, 140–150	21.60	3.2	0.30
4H-2, 140–150	26.60	2.6	0.53
4H-5, 140–150	31.10	1.2	0.43
5H-2, 140–150	36.10	0.3	0.42
5H-5, 140–150	40.60	3.5	0.15
6H-2, 140–150	45.57	3.6	0.31
6H-5, 140–150	50.00	2.9	–0.11
7H-2, 130–140	54.89	3.4	0.09
7H-5, 140–150	59.39	3.0	0.19
8H-2, 140–150	64.60	1.7	0.18
8H-4, 0–25	66.20	6.9	0.69
8H-5, 140–150	69.10	2.6	–0.05
9H-2, 140–150	73.81	–0.4	–0.03
9H-5, 140–150	78.31	1.9	–0.01
9H-7, 52–68	79.93	2.5	0.07
10H-2, 140–150	83.60	2.2	–0.14
10H-5, 132–142	88.02	1.9	–0.22
11H-2, 140–150	93.10	3.3	–0.41
11H-5, 83–93	96.54	1.9	–0.18
12H-2, 140–150	102.60	1.5	–0.28
12H-4, 67–87	104.87	3.9	0.16
12H-5, 0–20	105.47	2.4	–0.16
12H-5, 20–36	105.67	0.3	–0.15
13H-2, 135–150	112.05	0.8	–0.74
13H-5, 135–150	116.55	0.9	–0.48
14H-2, 135–150	121.55	1.9	–0.57
15H-2, 140–150	125.15	1.7	–0.53
15H-4, 140–150	128.15	3.8	
16H-2, 140–150	132.70	3.0	–0.14
204-1247B-			
1H-1,140–150	1.40	0.5	0.58
1H-2, 90–100	2.40	–0.7	0.61
2H-1, 140–150	5.00	–0.4	0.57
2H-2, 140–150	6.50	–2.0	0.61
2H-3, 140–150	8.00	–2.0	0.35
2H-4, 140–150	9.50	1.1	0.46
2H-5, 140–150	11.00	0.4	0.52
2H-6,140–150	12.50	–1.5	0.15
2H-7, 77–78	13.37	2.6	0.42
3H-1, 140–150	14.50	2.6	0.39
3H-2, 140–150	16.00	1.7	0.51
3H-4, 140–150	19.00	1.0	0.38
5H-2, 140–150	27.50	0.7	0.25
5H-5, 140–150	32.00	–0.4	0.31
6H-2, 140–150	37.00	–0.4	0.52
6H-5, 140–150	41.50	3.0	0.38
7H-2, 140–150	46.45	2.4	0.05
7H-5, 140–150	50.95	4.5	0.26
8H-2, 140–150	56.00	4.0	0.37
8H-5, 140–150	60.50	4.3	0.04
9H-2, 140–150	65.41	2.4	0.24
9H-5, 140–150	69.91	1.7	0.18
10H-2, 140–150	75.00	–0.6	–0.16
10H-5, 140–150	79.50	–0.3	–0.12
11H-5, 140–150	88.61	–1.9	–0.13
12H-3, 140–150	94.51	2.0	0.06
12H-5, 140–150	97.51	2.2	–0.04
13H-2, 140–150	103.13	3.6	0.14
13H-3, 140–150	104.63	2.9	–0.30
14H-2, 140–150	109.60	2.8	–0.18
14H-5, 62–83	113.32	2.6	0.10
15X-1, 135–150	114.95	1.8	–0.41
15X-2, 135–150	116.45	1.1	0.15
18X-2, 135–150	130.15	–0.1	–0.16
18X-5, 135–150	134.65	–2.1	–0.02
19X-2, 127–147	137.37	2.7	–0.10
19X-5, 130–150	141.87	1.8	–0.32
20X-3, 130–150	148.50	2.9	–0.17
22X-3, 130–150	167.80	4.1	–0.53
23X-3, 130–150	177.40	2.9	–0.63
24X-3, 130–151	187.00	10.1	–0.50
25X-3, 130–151	196.33	1.0	–0.36
26X-3, 130–151	206.20	–0.8	–0.10
27X-3, 130–151	215.50	–1.7	–0.26
204-1248B-			
1H-1, 0–20	0.00	–2.4	0.63
1H-2, 0–20	1.20	1.7	0.43
2H-1, 77–87	7.27	4.7	0.33
2H-3, 91–101	9.16	6.0	0.34
204-1248C-			
1X-1, 138–148	1.38	6.6	0.86
2X-CC, 0–15	10.68	4.7	0.08
3X-1, 140–150	20.60	2.2	0.04
5X-1, 140–150	39.80	1.6	–0.21
5X-CC, 18–28	41.18	–0.5	–0.14
6H-3, 129–139	51.05	–1.7	–0.27
6H-5, 140–150	53.84	–1.4	–0.11
7H-2, 140–150	60.40	1.5	–0.21
7H-5, 140–150	64.90	1.5	–0.20
8H-2, 137–147	69.87	1.7	–0.23
8H-CC, 0–10	74.65	3.5	–0.17
9H-2, 140–150	79.40	2.9	–0.32
9H-5, 140–150	83.90	2.3	–0.30
10H-2, 135–150	88.54	3.9	0.09
10H-5, 112–127	92.73	2.5	–0.07
11H-2, 135–150	97.51	3.0	–0.06
11H-4, 122–137	100.36		0.15
12H-2, 131–146	107.81	1.5	0.05
12H-5, 135–150	111.96	2.7	–0.08
13H-2, 135–150	117.33	3.8	–0.04
13H-4, 132–147	120.21	2.8	0.03
14H-2, 135–150	125.62	2.4	–0.08
15H-2, 85–100	135.30	2.4	–0.19
16H-1, 135–150	137.85	2.7	–0.28
16H-3, 135–150	140.85	2.1	–0.25
17X-1, 135–150	143.35		–0.27
17X-3, 135–150	146.35	2.6	–0.22
204-1249B-			
2A-1, 45–60	30.35	1.4	–0.05
2A-2, 112–126	31.82	3.4	0.16
3A-1, 31–46	34.71	2.5	0.29
4A-1, 78–93	39.43	4.6	0.13
5A-1, 78–93	44.18	2.2	0.04
6A-2, 95–106	49.85	2.9	0.01
7A-1, 42–57	52.82	0.8	–0.04
204-1249C-			
1H-1, 118–125	1.18	–3.1	–0.15
2H-2, 0–15	3.40	–2.1	0.03
2H-2, 15–30	3.55	–2.2	–0.05
3H-1, 74–89	5.74	2.0	0.41
3H-2, 41–51	6.96	–2.2	0.16
4H-2, 44–62	15.77	0.4	0.58
4H-5, 86–101	17.61	1.5	0.15
5H-2, 20–25	25.70	2.3	0.05
5H-4, 44–49	27.70	0.5	0.11
7H-1, 71–86	35.71		0.06
7H-5, 76–91	38.89	2.6	0.12
8H-3, 18–33	47.64	1.8	–0.04
8H-4, 124–139	50.18	5.0	0.16
9H-2, 133–148	56.83	2.4	–0.19
9H-3, 120–135	58.18	2.4	–0.07
11H-4, 104–119	69.17	2.6	–0.23
11H-6, 95–115	71.74	6.9	0.29
12H-1, 120–140	75.70	6.3	–0.23
13H-2, 79–99	86.29	0.8	–0.17
204-1249D-			
1H-2, 25–40	1.52		0.51
3H-1, 79–94	9.79	2.7	0.48
204-1249F-			
3H-1, 45–47, by hydrate (dry)	9.45	–4.3	–0.61
3H-1, 76–78, by hydrate (wet)	9.76	–1.8	–0.31
3H-1, 76–78, by hydrate (dry)	9.76	–5.6	–0.75
3H-2, 33–35, by hydrate (wet)	10.33	0.0	–0.09
3H-2, 33–35, by hydrate (dry)	10.33	–5.4	–0.56
7H-1, 28–30, by hydrate	21.18	3.5	0.30
7H-1, 48–50, by hydrate	21.38	1.9	–0.05
7H-1, 67–69, by hydrate	21.57		–0.03
7H-2, 106–116	23.41	2.6	0.11
9H-3, 140–150	43.61	3.4	0.14
10H-2, 140–150	52.09	2.8	–0.32
12H-2, 131–146	63.20	2.2	–0.17
15H-5, 135–150	79.57	2.8	–0.27
16H-4, 135–150	88.50	1.6	–0.55
204-1250C-			
1H-1, 0–10	0.00	1.7	0.25
2H-CC, 1–10	5.07		0.08
3H-2, 140–150	16.90	2.1	0.24
3H-5, 140–150	21.40	2.6	0.17
4H-2, 140–150	26.40	1.7	0.22
4H-4, 140–150	29.00	4.7	0.15
5H-2, 140–150	35.88	3.3	0.08
5H-5, 133–143	40.31	2.2	0.18
6H-2, 57–67	44.57	6.8	0.07
6H-5, 118–128	48.95	1.6	0.04
7H-5, 130–140	58.00	2.6	0.01
8H-2, 140–150	64.40		–0.15
8H-5, 140–150	68.90	2.1	–0.05
10H-2, 81–96	75.31	3.4	–0.18
10H-5, 135–150	79.81	2.2	–0.04
11H-3, 95–110	86.36	0.5	–0.11
11H-5, 130–150	89.31	1.7	–0.16
12H-1, 50–65	92.50	2.4	–0.10
12H-5, 140–155	98.43	3.6	–0.12
13H-2, 130–150	103.98	1.8	–0.19
13H-5, 130–150	108.48	3.1	–0.11
14H-2, 130–150	113.80		–0.12
14H-4, 40–60	115.33	1.5	–0.16
15H-1, 106–126	121.56	1.8	–0.05
15H-4, 100–120	125.86	1.0	–0.15
17H-1, 130–150	133.30	3.9	–0.01
17H-3, 130–150	136.30	3.3	–0.21
19X-2, 130–150	141.30	1.8	–0.15
19X-5, 130–150	145.75	2.6	–0.19
204-1250D-			
3H-4, 52–62	21.02	0.3	0.14
3H-7, 140–150	24.90	1.9	0.05
4H-5, 140–150	32.90		0.18
6H-5, 129–144	44.24	1.2	0.01

Table T1 (continued).

Core, section, interval (cm)	Depth (mbsf)	δD (‰)	δ18O (‰)
8H-5, 130–150	61.48	1.5	–0.11
10H-5, 140–150	81.22	1.1	–0.13
12H-5, 0–20	99.75	2.1	–0.16
14H-4, 0–20	109.83	2.9	–0.04
15X-5, 0–25	120.91	2.6	–0.17
16X-4, 130–150	130.32	2.0	–0.18
19X-5, 130–150	144.50	1.8	–0.16
204-1250E-			
1H-1, 140–150	1.40	–2.1	0.16
1H-2, 131–141	2.81	0.3	0.52
2H-5, 140–150	13.90	–4.3	0.17
204-1250F-			
1H-2, 122–142	101.55	4.3	–0.12
1H-3, 130–150	103.05	3.4	–0.07
1H-4, 130–150	104.55	2.4	–0.20
1H-5, 130–150	106.05	5.1	–0.20
1H-6, 130–150	107.55	3.2	–0.19
2H-1, 130–150	110.80	1.4	–0.12
2H-2, 130–150	112.30	2.5	–0.05
2H-3, 69–89	113.19	1.4	–0.22
3X-1, 130–150	114.80	2.2	–0.05
3X-3, 130–150	117.80	2.7	–0.09
5H-1, 130–150	122.30	3.4	–0.07
5H-2, 130–150	123.80	3.5	–0.06
6X-1, 130–150	128.60	2.9	–0.19
6X-2, 100–120	129.80	4.8	0.00
9X-2, 130–150	136.80	3.3	–0.05
9X-5, 130–150	141.30	3.4	0.02
10X-1, 130–150	144.90	2.7	–0.04
10X-3, 130–150	147.90	1.3	–0.14
11X-2, 98–123	155.68	1.3	–0.29
12X-3, 125–150	167.05	2.6	–0.13
13X-3, 125–150	176.65	2.6	–0.07
204-1251B-			
1H-2, 145–150	2.95	1.2	0.13
1H-5, 145–150	7.45	3.2	0.30
3H-2, 140–150	21.43	3.4	0.34
3H-4, 140–150	24.41	3.9	0.32
4H-2, 140–150	31.00	3.0	0.33
4H-5, 140–150	35.50	1.8	0.33
5H-2, 131–141	40.41	1.4	0.04
5H-5, 138–150	44.84	–1.7	–0.01
6H-2, 130–140	49.22	4.1	0.07
6H-5, 131–141	53.61	2.1	0.01
7H-2, 140–150	59.50	–9.3	–0.12
7H-5, 140–150	64.00	3.0	–0.03
8H-2, 140–150	69.00	2.2	–0.03
8H-5, 140–150	73.38	–1.6	–0.16
10H-2, 140–150	88.00	–0.4	–0.10
10H-4, 140–150	91.00	–3.0	–0.18
11H-2, 74–94	96.84	1.0	–0.13
11H-5, 70–90	100.74	0.6	–0.13
13H-2, 130–150	108.55	1.6	–0.18
13H-5, 130–150	112.85	1.1	–0.10
14H-2, 130–150	117.91	–1.9	–0.22
14H-5, 130–150	122.41	–0.4	–0.18
15H-5, 124–144	132.34	–1.0	–0.23
16H-2, 130–150	137.40	–3.2	–0.32
16H-5, 121–141	141.81	–2.6	–0.20
17H-2, 130–150	146.90	–1.9	–0.26
17H-5, 80–100	150.90	–2.9	–0.26
19H-2, 130–150	158.16	–1.6	–0.31
19H-4, 130–150	161.08	–2.1	–0.37
20H-2, 130–150	165.98	–4.1	–0.31
20H-5, 130–150	170.48	–3.5	–0.42
22H-2, 130–150	175.50	–3.6	–0.37
22H-4, 128–148	178.48	–2.7	–0.33
23H-2, 130–150	185.00	–3.3	–0.37
23H-4, 102–122	187.72	–4.6	–0.49
26X-2, 130–150	205.83	–3.6	–0.39
26X-4, 130–150	209.88	–3.8	–0.41
27X-2, 125–150	216.25	–2.6	–0.42
27X-5, 125–150	220.75	–6.9	–0.46
28X-2, 125–150	225.85	–3.0	–0.41
28X-4, 125–150	228.85	–3.4	–0.44
29X-2, 125–150	235.55	–4.4	–0.43
30X-2, 125–150	245.15	–4.8	–0.48
30X-4, 110–135	248.00	–4.9	–0.44
31X-2, 116–141	254.76	–6.8	–0.36
32X-2, 125–150	264.45	–5.2	–0.44
33X-2, 125–150	274.05	–4.7	–0.37
33X-5, 125–150	278.55	–5.0	–0.41
34X-2, 128–148	283.78	–4.2	–0.47
34X-5, 130–150	288.13	–6.0	–0.42
36X-2, 130–150	295.40	–5.7	–0.42
36X-5, 80–100	299.40	–6.0	–0.56
37X-3, 120–150	304.80	–6.5	–0.63
38X-3, 130–150	314.60	–8.6	–0.55
39X-3, 130–150	324.20	–8.7	–0.51
41X-2, 130–150	333.40	–9.4	–0.49
42X-3, 130–150	343.50	–6.2	–0.55
43X-2, 130–150	350.43	–5.4	–0.52
44X-3, 130–150	362.70	–5.3	–0.53
45X-3, 130–150	372.30	–8.3	–0.56
46X-3, 130–150	381.90	–7.4	–0.65
47X-3, 130–150	391.60	–7.9	–0.64
49X-3, 130–150	402.20	–7.6	–0.57
50X-3, 130–150	410.80	–11.2	–0.74
51X-3, 130–150	420.50	–8.1	–0.69
52X-3, 130–150	430.10	–7.8	–0.55
53X-3, 130–150	439.78	–7.2	–0.58
204-1251C-			
1H-2, 140–150	2.90	0.2	0.24
1H-5, 140–150	7.40	3.2	0.25
2X-1, 140–150	9.50	1.9	0.31
2X-3, 140–150	12.07	2.7	0.33
204-1251D-			
1X-1, 140–150	1.40	0.7	0.20
1X-2, 90–100	2.40	2.0	0.24
2X-1, 140–150	9.50	2.8	0.26
2X-3, 50–60	11.10		
3X-2, 140–150	20.50	4.2	0.37
3X-4, 140–150	23.50	1.6	0.33
4H-2, 140–150	29.80	4.1	0.37
4H-4, 140–150	32.80	4.7	0.43
5H-5, 0–10	42.40	2.8	0.29
7H-3, 135–150	52.07	4.0	0.19
8H-5, 135–150	64.75	3.9	0.08
11H-4, 0–15	82.29	0.5	–0.10
11H-4, 135–150	83.06	1.9	–0.11
13H-6, 0–20	103.67	1.1	–0.05
15H-5, 0–15	122.40	0.4	–0.01
17H-5, 0–15	141.40	–1.5	–0.08
19H-2, 130–150	156.31	–1.3	–0.02
19H-5, 130–150	160.81	–1.1	–0.06
20H-2, 125–150	166.13	–1.2	–0.20
20H-5, 125–150	170.63	–0.5	–0.43
22X-1, 20–40	175.60	–0.8	–0.41
22X-2, 0–20	176.87	–1.2	–0.39
23X-2, 122–147	181.82	–1.4	–0.39
23X-3, 125–150	183.32	–2.1	–0.28
24X-2, 0–25	189.62	–1.2	–0.06
24X-3, 0–10	191.12	–0.6	0.13
24X-3, 140–150	192.52	–0.1	–0.01
24X-4, 43–63	193.05	0.9	0.09
25X-2, 125–150	200.95	–3.0	–0.24
25X-5, 125–150	205.45	–1.6	–0.27
26X-3, 125–150	210.43	–1.5	–0.27
204-1251E-			
1H-1, 85–95	0.85	0.2	0.25
1H-1, 140–150	1.40	0.9	0.24
1H-2, 80–90	2.30	1.2	0.16
1H-2, 140–150	2.90	2.9	0.29
1H-3, 60–70	3.60	0.9	0.40
1H-3, 140–150	4.40	1.6	0.17
1H-4, 60–70	5.10	1.5	0.44
1H-4, 140–150	5.90	0.4	0.33
204-1252A-			
1H-1, 135–150	1.35	0.5	0.10
1H-2, 135–150	2.85	2.2	0.15
1H-3, 85–100	3.85	1.4	0.22
2H-1, 135–150	6.25	3.4	0.33
2H-2, 135–150	7.75	1.3	0.18
2H-3, 135–150	9.25	4.2	0.24
2H-4, 135–150	10.75	1.6	0.27
2H-5, 135–150	12.25	2.4	0.29
2H-6, 135–150	13.75	4.0	0.34
3H-2, 135–150	16.00	4.6	0.23
3H-5, 135–150	20.50	4.5	0.25
4H-2, 135–150	26.75	5.1	–0.06
4H-5, 135–150	31.13	3.7	0.19
5H-2, 135–150	35.34	3.8	0.16
5H-5, 135–150	39.84	2.0	0.19
6H-2, 135–150	45.75	2.9	0.10
6H-5, 135–150	50.25	2.6	0.00
7H-2, 135–150	55.25	–1.8	–0.03
7H-5, 135–150	59.75	2.1	–0.15
8H-2, 135–150	64.75	2.2	–0.25
8H-5, 135–150	69.25	2.5	–0.07
9H-2, 135–150	74.25	1.9	–0.11
9H-5, 135–150	78.75	1.4	–0.14
10H-2, 45–60	82.85	1.3	–0.26
10H-5, 135–150	87.35	1.6	–0.32
11H-2, 135–150	93.25	–1.2	–0.18
11H-6, 80–95	98.70	0.2	–0.18
12H-2, 135–150	102.75	–2.6	–0.29
12H-5, 135–150	107.15	0.5	–0.36
13H-2, 135–150	112.25	–0.9	–0.45
13H-4, 67–87	114.57	–0.1	–0.30
14H-2, 135–150	121.75	0.1	–0.33
14H-5, 102–127	125.84	–0.2	–0.35
15X-2, 135–150	127.85	–1.5	–0.43
15X-5, 130–150	132.18	–1.0	–0.36
16X-2, 130–150	137.50	–1.9	–0.35
16X-4, 130–150	140.50	–1.2	–0.55
17X-2, 130–150	147.20	–1.3	–0.53
17X-5, 130–150	151.70	–1.3	–0.50
18X-2, 130–150	156.90	–1.4	–0.43
18X-4, 130–150	159.90	–1.3	–0.38
19X-2, 130–150	166.60	–1.9	–0.58
19X-5, 130–150	171.10	–2.2	–0.53
20X-2, 130–150	176.30	–3.4	–0.62
20X-3, 130–150	177.80	–3.2	–0.58
21X-2, 130–150	185.90	–3.7	–0.67
21X-5, 130–150	190.40	–3.8	–0.60
22X-3, 130–150	197.00	–3.1	–0.86
23X-3, 130–150	205.78	–3.0	–0.65
24X-3, 130–150	215.50	–2.5	–0.83
25X-3, 130–150	225.20	–2.8	–0.76
26X-3, 130–150	234.80	–2.5	–0.91
27X-3, 130–150	244.50	–3.6	–0.91
28X-3, 130–150	254.14	–4.6	–0.96

Note: This table is also available in ASCII.